symmetry

MDPI

Article

Research on Vibration and Noise of Induction Motor under Variable Frequency

Zhonghuan Su [1,2], Longfu Luo [1], Jun Liu [1], Zhongxiang Li [1], Hu Luo [1] and Haonan Bai [3,*]

[1] College of Electrical and Information Engineering, Hunan University, Changsha 410012, China; zhonghuansu@163.com (Z.S.); longfuluo852@163.com (L.L.); junliu72@163.com (J.L.); zhongxiangli1215@163.com (Z.L.); huluo211@163.com (H.L.)
[2] TBEA Hengyang Transformer Co., Ltd., Hengyang 421007, China
[3] Key Laboratory of Special Motors and High Voltage Electrical Appliances, Ministry of Education, Shenyang University of Technology, Shenyang 110178, China
* Correspondence: baihaonan@smail.sut.edu.cn; Tel.: +86-183-4089-9486

Abstract: Studies have substantiated that the vibration and noise produced by the iron core of an electromagnetic device are closely related to the magnetostriction of the iron core silicon steel sheet. Moreover, when the induction motor works under the condition of frequency conversion, the symmetry of the core silicon steel sheet will change, and the distribution of the vibration and noise field of the motor will be asymmetric, which will aggravate the vibration and noise. This paper completes the experimental measurement and analysis of the electromagnetic characteristics and magnetostrictive characteristics of silicon steel sheets. The magnetic field of a 1140 V/75 kW variable-frequency motor is calculated analytically based on the analytical method, and the stator/rotor magnetic induction intensity and permeance are calculated separately to obtain the air gap magnetic density and the radial electromagnetic force. The vibration and noise of the 1140 V/75 kW variable-frequency motor are analyzed by the finite element method, while the magnetization curve and magnetostrictive characteristic curve of a silicon steel sheet under different conditions are considered. An experimental platform is built to measure and analyze the vibration displacement and acceleration of the variable frequency motor, which verifies the correctness of the proposed scheme. Considering the influence of the magnetostrictive effect will make the result of calculating the vibration and noise of variable-frequency motors more accurate.

Keywords: frequency conversion; induction motor; magnetostriction; vibration and noise; analytical method; finite element method; simulation and experiment

check for updates

Citation: Su, Z.; Luo, L.; Liu, J.; Li, Z.; Luo, H.; Bai, H. Research on Vibration and Noise of Induction Motor under Variable Frequency. *Symmetry* **2022**, *14*, 569. https://doi.org/10.3390/sym14030569

Academic Editors: Wenliang Zhao, Dezhi Chen and Jinhua Chen

Received: 26 November 2021
Accepted: 10 February 2022
Published: 14 March 2022

Publisher's Note: MDPI stays neutral with regard to jurisdictional claims in published maps and institutional affiliations.

Copyright: © 2022 by the authors. Licensee MDPI, Basel, Switzerland. This article is an open access article distributed under the terms and conditions of the Creative Commons Attribution (CC BY) license (https://creativecommons.org/licenses/by/4.0/).

1. Introduction

In recent years, the AC variable-frequency speed-regulation system has become the most promising speed control method, gradually replacing the DC speed control system with its excellent speed control performance, significant power saving effect, and wide applicability in various fields of the world economy [1]. However, the vibration and noise produced cannot be ignored.

Studies have substantiated that one of the reasons for the vibration and noise of the induction motor powered by a variable frequency is the magnetostrictive effect of the iron core [2]. In [3], Fan, W. studied the dynamic model and analysis method of the transmission process of DCDS. In [4], Maraaba, L.S. presented a novel method for the stator inter-turn fault diagnosis of a wire-started PMSM, which utilizes frequency analysis of the acoustic signals caused by asymmetric faults. In [5], Chang, Y. H. studied the core vibration of a transformer based on the measurement results of the magnetostriction of silicon steel sheets and gave a mathematical calculation model of magnetostrictive force and electromagnetic force. In [6], O. A. Mohammed studied the deformation of the motor stator caused by the magnetostrictive effect of the silicon steel sheet. In [7], K. Delaere

studied the magnetostrictive force by measuring the strain of the motor stator, and then calculated the vibration of the motor based on the thermal stress micro-displacement finite element method and analyzed the vibration frequency spectrum. At the same time, the electromagnetic design and manufacturing process of the motor will also affect the vibration and noise of the motor. In [8], M. Islam studied the vibration and noise of fractional-slot permanent magnet motors with variant pole-slot ratios. In [9], D. Fodorean calculated the vibration frequency and noise of a DC motor and a permanent magnet motor and concluded that permanent magnet motors are more suitable for a number of low-noise applications than DC motors. In another study [10], starting from the stiffness of the motor stator, L. Gao analyzed the radial electromagnetic force wave and the harmonic response of the motor stator by an analytical method and the finite element method, and the vibration and noise of a 48-slot, eight-pole motor were simulated. In [11], based on a special dual-branch three-phase permanent magnet synchronous motor (PMSM), W. Deng presented a method that utilizes a known modified space vector PWM technique that can suppress unpleasant high-frequency vibration noise as well as acoustic noise more effectively than other methods. In [12], Han, Z. found that the zeroth-spatial-order axial force is dominant for the generation of the vibration and noise in axial-flux motors. In [13], the performance of the vibration and noise under classical field-oriented control, offline MTPA control, and online MTPA control was investigated.

Researchers have conducted a great deal of research on motor vibration and noise-related issues, but there are few studies on motor silicon steel sheet magnetostriction at different temperatures and frequencies.

Variable-frequency motors usually work under conditions of high temperatures, poor power supply quality, and variable load conditions. Silicon steel sheet manufacturers usually only provide the magnetic characteristic data curve of silicon steel sheets at room temperature and power frequency, which does not reflect the actual operating conditions of the variable-frequency motor. Therefore, it is of great significance to investigate the magnetic properties of the stator core materials of variable-frequency motors resulting in various temperatures and harmonics.

This article considers a frequency conversion motor with a laminated core of a silicon steel sheet and studies its vibration and noise; the electromagnetic force and the magnetostriction of the silicon steel sheet are considered comprehensively. This paper is organized as follows. Firstly, the magnetic properties and magnetostrictive properties of a non-oriented silicon steel sheet under different temperatures and harmonics are described. Secondly, the electromagnetic force wave of the variable-frequency motor is calculated; then, the vibration and noise of the 1140 V/75 kW variable-frequency motor are simulated and analyzed by multi-physics coupling, and the vibration test is verified. This paper provides a relatively novel method for calculating the vibration and noise of variable-frequency motors and provides theoretical support and a reference for the design of low-noise motors.

2. Analysis of the Magnetic Properties of Non-Oriented Silicon Steel Sheets at Variant Temperatures and Frequencies

The magnetic properties of non-oriented silicon steel sheets will affect the performance of the motor [14]. This paper analyzes the electromagnetic characteristics of the stator core silicon steel sheet of a 1140 V/75 kW variable-frequency motor that is used in coal mines at varied temperatures and different harmonics, and gives the magnetic performance data of silicon steel sheets under dissimilar temperatures and harmonics.

2.1. Measuring Principle

Figure 1 shows the device for measuring the magnetic properties of silicon steel sheets. The device is mainly used to measure the magnetic properties of various soft magnetic materials. The system complies with IEC (IEC60404 and IEC60205) and ASTM standards. In the experiment, the working temperature of the silicon steel sheets was adjusted by the temperature control system, and the input waveform of the silicon steel sheets was

adjusted by the excitation power supply. We obtained the *B-H* data, *B-P* data, and magnetic permeability data of the silicon steel sheets through the data acquisition system.

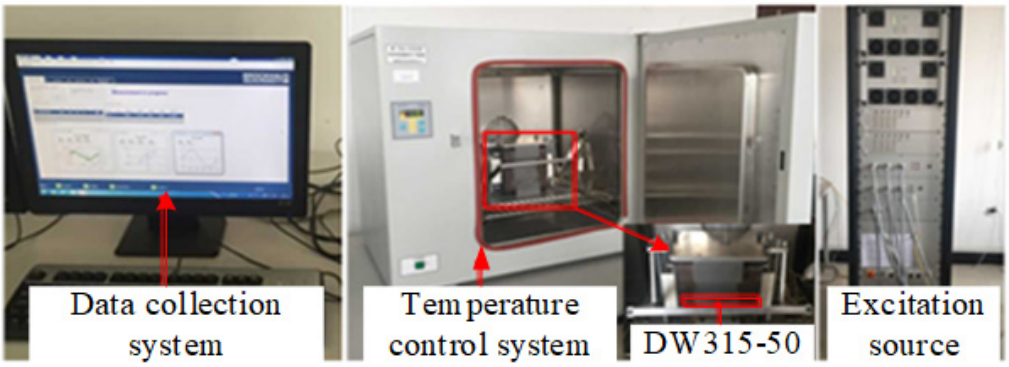


Figure 1. The system of test insulation for magnetic characteristics of silicon steel sheet.

Figure 2 provides a sectional view of the magnetic property measuring device for silicon steel sheets. The experiment used the single-chip measurement principle to measure the magnetic properties of silicon steel sheets under different temperatures and harmonic conditions. The sample was placed in the center of the coil skeleton and formed a closed magnetic circuit with the iron yoke, which was formed by stacking the silicon steel sheets. For the sake of evenly distributing the magnetic field applied to the sample, there had to be a sufficient contact area between the sample and the iron yoke. In addition, the "B coil" was the magnetic induction intensity measuring coil, and the "H coil" was the magnetic field intensity measuring coil; the "B coil" and the excitation coil were evenly wound on the coil skeleton in two layers. The "H coil" was evenly wound on a plate-shaped support composed of non-magnetically conductive insulating material and as close as possible to the sample.

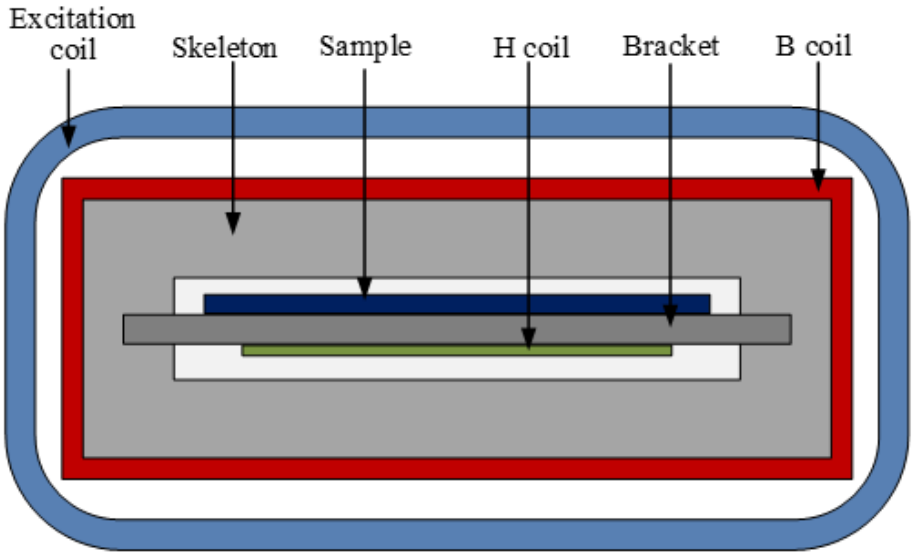


Figure 2. Single sheet tester section view.

In further analysis, the data acquisition part of the silicon steel sheet magnetic characteristic test system converted the voltage collected by the excitation coil, H coil, and B coil into the magnetic field strength, which can be expressed as follows:

$$H(t) = \frac{N_1 I(t)}{l_m} = \frac{N_1 u_1(t)}{R_n l_m}, \quad (1)$$

At the same time, the magnetic induction intensity can be obtained from the collected B coil voltage, and it can be expressed as follows:

$$\frac{dJ}{dt} = -\frac{u_2(t)}{N_2 A_m} \Rightarrow J(t) = -\frac{1}{N_2 A_m}\int_0^t u_2(t)dt, \quad (2)$$

where $H(t)$ is the magnetic field strength, N_1 is the number of primary windings, $I(t)$ is the primary current, l_m is the length of the magnetic circuit, $u_1(t)$ is the primary voltage, R_n is the equivalent resistance, $u_2(t)$ is the secondary side voltage, N_2 is the number of secondary windings, A_m is the equivalent area, and $J(t)$ is the magnetic induction intensity.

The performance parameters of the monolithic silicon steel sheet measuring device are shown in Table 1.

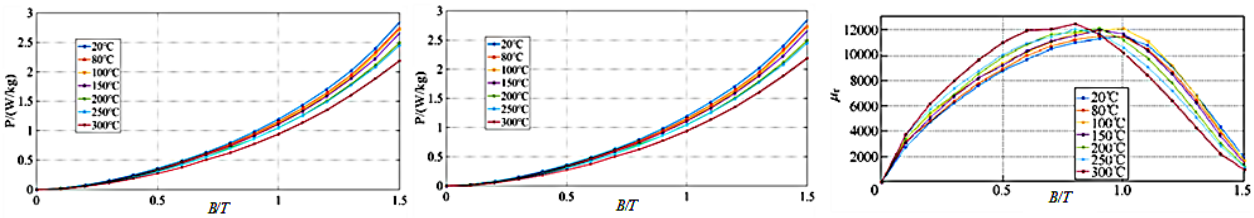
Table 1. Performance parameters of single-piece silicon steel sheet measuring device.

Parameter	Value	Precision (%)
Temperature/°C	20~300	-
Sample size (length × width × height)/mm	150 × 150 × 0.5	-
Magnetic field strength/(A/m)	10,000	0.2
Magnetic induction/T	0.001~2	0.2
Frequency/Hz	1~5000	-

2.2. Analysis of the Magnetic Performance Test Results of Non-Oriented Silicon Steel Sheets

2.2.1. Test and Analysis of Magnetic Properties of Non-Oriented Silicon Steel Sheets at Separate Temperatures

Figure 3 shows the B-H curve, B-*p* curve, and magnetic permeability curve of the non-oriented silicon steel sheet at different temperatures.



(**a**) (**b**) (**c**)

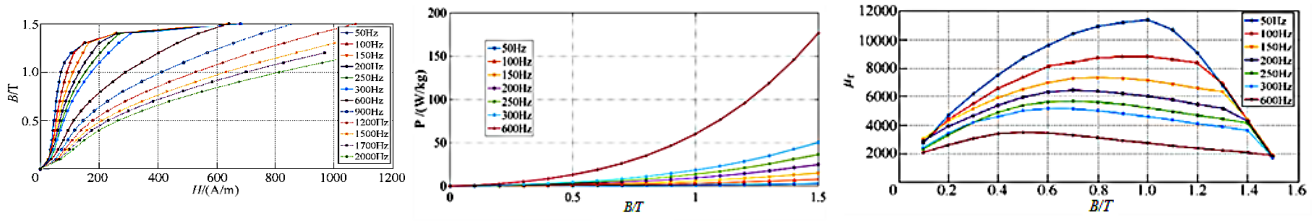
Figure 3. B-H curves, B-*p* curves, and magnetic permeability curves of silicon steel sheets at diverse temperatures: (**a**) B-H curve of silicon steel sheet at different temperatures; (**b**) B-*p* curve of silicon steel sheet at different temperatures; (**c**) permeability curve of silicon steel sheet at different temperatures.

As can be seen from Figure 3a–c, with the increase in temperature, the working point of the non-oriented silicon steel shifted to the right, the saturation magnetic induction intensity decreased, the loss of the silicon steel sheet decreased under the same magnetic induction intensity, and the permeability of the silicon steel sheet increased.

The results in Figure 3 show that the increase in temperature increased the activity of the magnetic domain change of the silicon steel sheet, and its hysteresis characteristics decreased, which in turn decreased the magnetic induction intensity and the loss, and caused the magnetic permeability to proliferate. The results demonstrate that temperature has a certain influence on the magnetic properties of silicon steel sheets. When using silicon steel sheets for electromagnetic product design, the influence of the working temperature should be considered.

2.2.2. Test and Analysis of Magnetic Characteristics of Non-Oriented Silicon Steel Sheets under Diverse Harmonics

The B-H curve, B-*p* curve, and permeability curve of silicon steel sheets under different harmonics are shown in Figure 4.



(**a**) (**b**) (**c**)

Figure 4. B-H curve, B-*p* curve, and magnetic permeability curve of silicon steel sheets under diverse harmonics: (**a**) B-H curve of silicon steel sheet under different harmonics; (**b**) B-*p* curve of silicon steel sheet under different harmonics; (**c**) permeability curve of silicon steel sheet under different harmonics.

As can be seen from Figure 4a–c, with the increase in frequency, the working point of the magnetic induction intensity of the silicon steel sheet shifts to the right, the saturated magnetic induction intensity and permeability of the silicon steel sheet decrease, and the loss of the silicon steel sheet increases. The above results show that the magnetic properties of silicon steel sheets deteriorate with the increase in frequency in the non-power frequency state.

2.3. Analysis of Magnetostrictive Properties of Non-Oriented Silicon Steel Sheets

Under the action of a magnetic field, not only will the electromagnetic properties of silicon steel sheets change, but also periodic expansion and contraction (magnetostrictive effect of silicon steel sheets) will occur. The expansion and contraction of silicon steel sheets will result in vibration and noise in the electromagnetic device. Based on the above assumptions, in this study, we tested the magnetostrictive properties of non-oriented silicon steel sheets. Figure 5 shows the magnetostriction measuring device for silicon steel sheets. The performance parameters of the silicon steel sheet magnetostrictive measuring device are shown in Table 2.

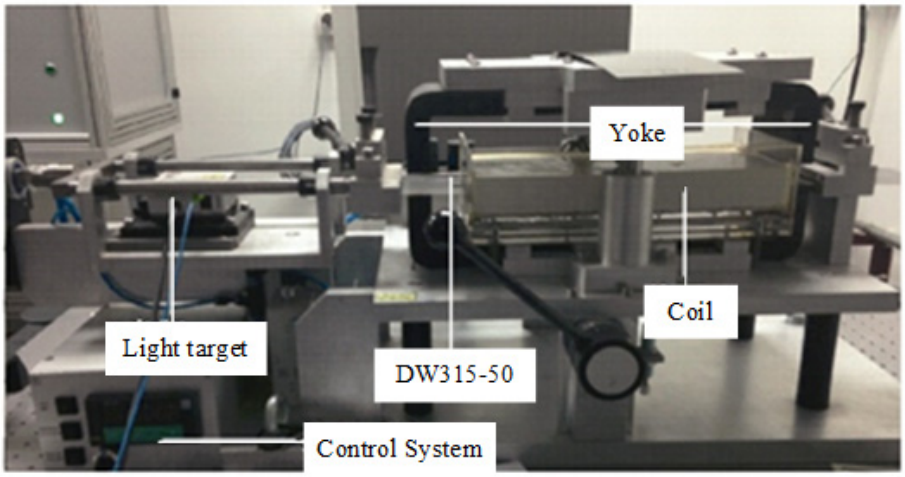


Figure 5. Silicon steel sheet magnetostrictive measuring device.

Table 2. Silicon steel sheet magnetostrictive measuring device performance parameters.

Project	Parameter
Silicon steel sheet model	DW315-50
AC excitation parameters	50 Hz, B_{peak} = 0.5~1.7 T

Figure 6 shows the B-H hysteresis loop of the silicon steel sheets, and Figure 7 shows the magnetostrictive butterfly curve of the silicon steel sheets. The values are shown in Figures 6 and 7. The magnetic induction intensity from inside to outside gradually increases, the hysteresis loop concerns the origin symmetry, and the butterfly curve refers to the Y-axis symmetry. In Figure 8, we show a single-value curve of silicon steel sheet magnetostriction.

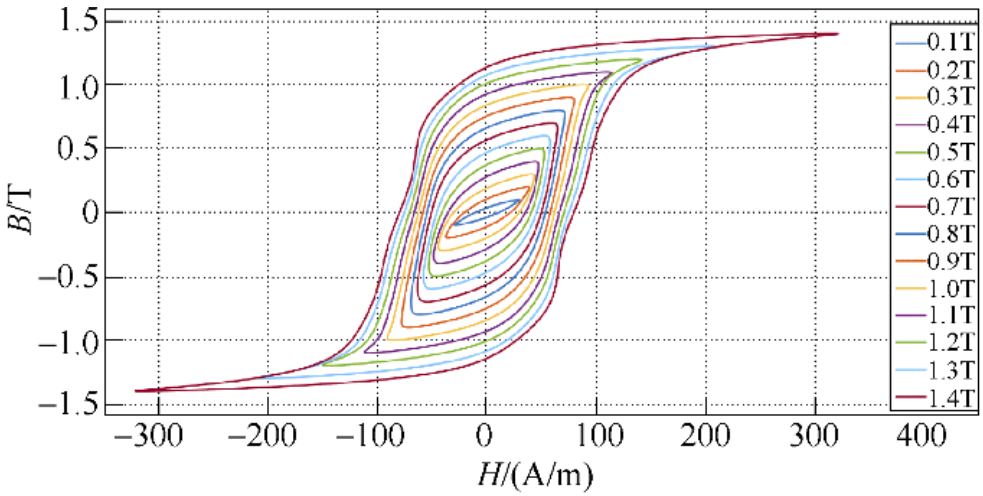


Figure 6. Silicon steel sheet B-H hysteresis loop.

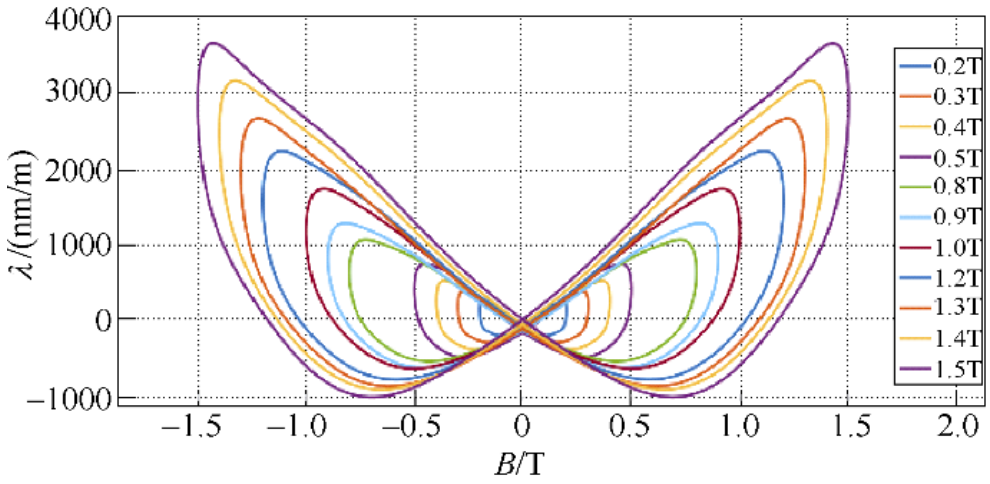
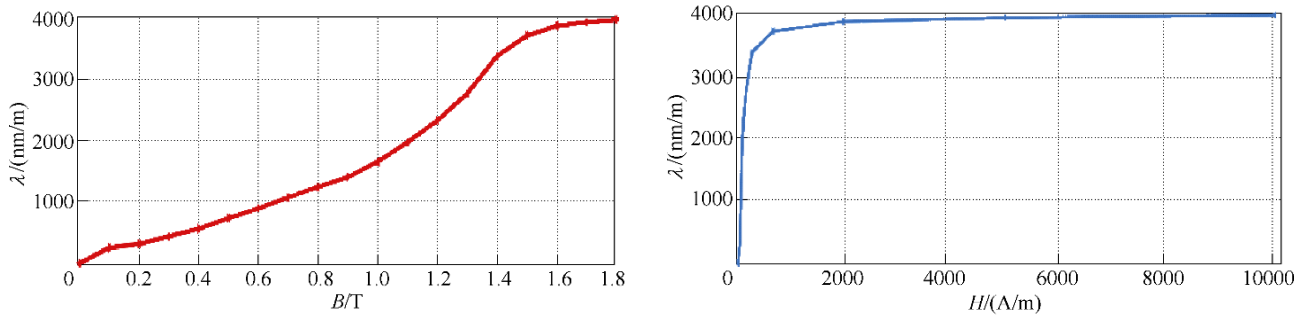


Figure 7. Silicon steel sheet magnetostrictive butterfly curves.



(**a**) (**b**)

Figure 8. B-H curve, B-*p* curve, and magnetic permeability curve of silicon steel sheets under diverse harmonics: (**a**) *B*-λ curve; (**b**) *H*-λ curve.

As shown in Figure 7, with the increase in magnetic induction intensity, the area of the magnetostrictive butterfly curve increases, i.e., the vibration of the silicon steel sheets intensifies. It can be seen from Figure 8 that when saturation is reached, the magnetostriction of the silicon steel sheets stabilizes at 4000 nm/m.

3. Analytical Modeling of Frequency Conversion Motor Core Vibration

For the purpose of mathematically expressing the vibration characteristics of variable-frequency motors, it is necessary to establish a mathematical model of motor vibration [15]. First, the stator magnetic potential and rotor magnetic potential of the variable-frequency motor are mathematically calculated. Second, the permeance wave is calculated; the electromagnetic force in the air gap is obtained by multiplying the stator and rotor magnetic potential with the magnetic conductivity. Finally, combined with the structure and material properties of the motor stator, the radial displacement and natural frequency of the motor vibration are calculated.

The air gap magnetic field of the motor will produce an electromagnetic force on the inner surface of the motor stator. By decomposing the electromagnetic force, two electromagnetic forces of different magnitudes, perpendicular to each other, can be obtained, namely the radial electromagnetic force and the tangential electromagnetic force. The radial electromagnetic force is the main result of motor vibration and noise, while the tangential electromagnetic force mainly produces the torque of the motor, and the contribution to the vibration and noise of the motor is relatively small; hence, the tangential electromagnetic force is often ignored and simplified in calculations. We used traditional mathematical analysis to model and calculate the vibration of the motor. Figure 9 shows a simplified schematic diagram of motor vibration.

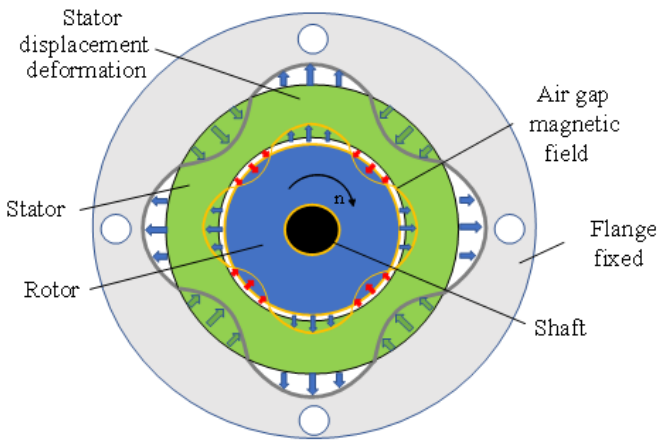


Figure 9. Simplified schematic diagram of motor vibration.

According to Maxwell's stress tensor law, the radial electromagnetic force acting on the unit area of the stator core of the motor or the waveform of the electromagnetic force wave in the air gap of the motor is proportional to the square of the air gap magnetic induction intensity. The equation is as follows:

$$P_n(\theta,t) = \frac{b^2(\theta,t)}{2\mu_0} = \frac{1}{2\mu_0}\left\{\frac{B_1^2}{2}\cos(2p\theta - 2\omega_1 t - 2\varphi_{0v}) + \sum_{v_z}\sum_{\mu_z} B_{v_z}B_{\mu_z}\cos[(\mu \pm v)\theta - (\omega_\mu \pm \omega_1)t - (\varphi_{u_z} \pm \varphi_{v_z})]\right\} \quad (3)$$

where $P_n(\theta,t)$ is the radial electromagnetic force, $b^2(\theta,t)$ is the air gap magnetic induction intensity, and μ_0 is the air permeability.

In Equation (3), the air gap magnetic induction is the product of the air gap magnetomotive force, and the relative air gap permeability, $b^2(\theta,t)$ can be formulated as follows:

$$b^2(\theta,t) = f(\theta,t)\lambda(\theta,t) \quad (4)$$

where $f(\theta,t)$ is the radial electromagnetic force and $\lambda(\theta,t)$ is the air gap permeance.

In the calculation, the force on the inner surface of the stator of the motor needs to be converted into the concentrated electromagnetic force acting on the stator teeth, as shown in Equation (5):

$$P_n' = 2\pi R_{1i} l_1 P_n \quad (5)$$

where R_{1i} represents the equivalent radius of the inner surface of the stator teeth, and l_1 is the length of the stator core.

The vibration displacement of the motor is not only related to the magnitude of the radial electromagnetic force but also closely related to the stiffness and mass of the motor stator and shell. The equations of concentrated stiffness and concentrated mass are as follows:

$$K = 16\pi\frac{E_c}{D_c^3}\frac{h_c^3 L_i}{D_c^3}(n^2-1)k_a^2 \quad (6)$$

$$m = G\frac{n^2+1}{n^2} \quad (7)$$

Table 3 shows the main parameters of motor and silicon steel sheet stiffness.

Table 3. Main parameters of motor and silicon steel sheet stiffness.

Parameter	Meaning	Value
E_c	the elasticity of the material	200 e^9
D_c	the average diameter	368 mm
h_c	the thickness of the core yoke	30 mm
L_i	the effective length of the core	310 mm
n	the order of the vibration force wave	2–4
k_a	the coefficient	2
G	total mass	316.2 kg

By calculating the radial electromagnetic force, concentrating stiffness, and concentrating mass, the vibration displacement of the motor and the natural frequency of the stator can be obtained. Since the closed motor stator and the shell are closely connected, the vibration displacement of the motor stator is the same as the vibration displacement of the shell. The equation can be expressed as follows:

$$Y_1 = Y_2 = \frac{P_n'}{K - \omega^2 m} \quad (8)$$

Stator natural frequency:

$$f_n = \frac{1}{2\pi}\sqrt{\frac{K}{m}} \tag{9}$$

Because the order of the force wave generated by the tooth harmonics of the stator and rotor is not overwhelmingly large, it is not the main source of vibration. The harmonic excitation force when $\mu = -36$ and $\nu = 38$ should be mainly considered, i.e., the vibration frequency and displacement analysis when $n = 2$.

Vibration force frequency:

$$f' = f[k_2\frac{Z_2}{p}(1-s)+2] \tag{10}$$

where $f = 50$ Hz, $k_2 = -1$, $Z_2 = 38$, $p = 2$, $s = (0.015)$ can obtain $f = 835.75$ Hz, $\omega = 2\pi f' = 5251$ rad/s.

Placing Equations (7)–(9) into Equation (3), one can calculate the vibration displacement of the induction motor. When the relevant parameters of the induction motor are changed, under the same excitation, the vibration displacement of the induction motor will change.

By summarizing the above formulas, we used computer programming for mathematical calculations, as described in this section. The distribution waveform of the air gap magnetic induction intensity on the circumference when the phase current reaches the maximum value is obtained, and then the radial vibration displacement of the motor is obtained, as substantiated in Figures 10 and 11.

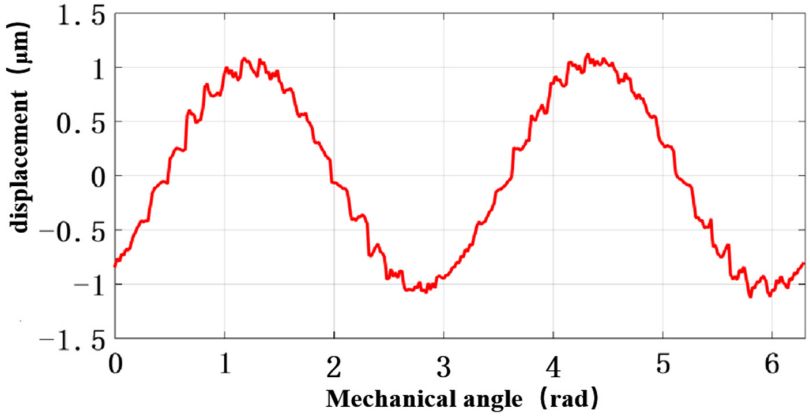


Figure 10. The calculation results of air gap magnetic induction.

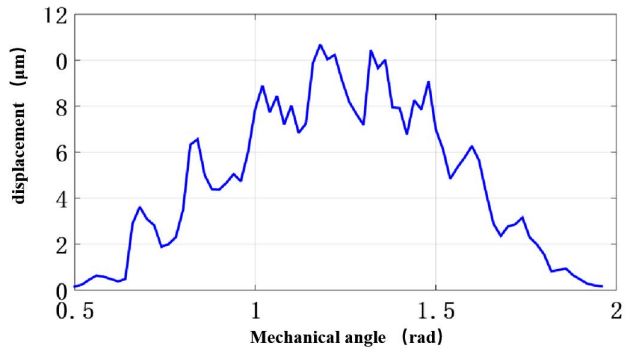


Figure 11. The calculation results of motor radial displacement.

In Figure 10, the magnetic induction intensity of the air gap of the motor is close to the sinusoidal distribution, and its maximum magnetic induction intensity is 1.1 T. As can be

seen in Figure 11, the vibration displacement of the motor changes with the change in the air gap magnetic induction, and the maximum displacement is around 10 μm.

4. Analysis of Electromagnetic Characteristics, Vibration, and Noise of Variable-Frequency Motors

In order to explore the influence of the electromagnetic characteristics of variable-frequency motors on vibration and noise, it is necessary to use finite element software for modeling and analysis [16]. Based on the COMSOL finite element software, we carried out a simulation analysis of the electromagnetic vibration and noise characteristics of the 1140 V/75 kW variable-frequency motor at different temperatures, dissimilar harmonics, and considering the magnetostrictive characteristics. The basic parameters of the variable-frequency motor are shown in Table 4.

Table 4. Variable-frequency motor basic parameters.

Parameter	Value
Rated power/kW	75
Rated voltage/V	1140
Rated current/A	48.32
Number of pole pairs	2
Rated speed/(r/min)	1478

Figure 12 shows the process of electromagnetic vibration and noise finite element analysis of variable-frequency motors. First, we established a finite element model of the variable-frequency motor; secondly, we input the distinguishing temperature, different harmonics, and magnetostrictive single-value curves into the finite element model, and simulated and analyzed the magnetic induction intensity, vibration, and noise of the variable-frequency motor; finally, the simulation and experiment were compared and analyzed.

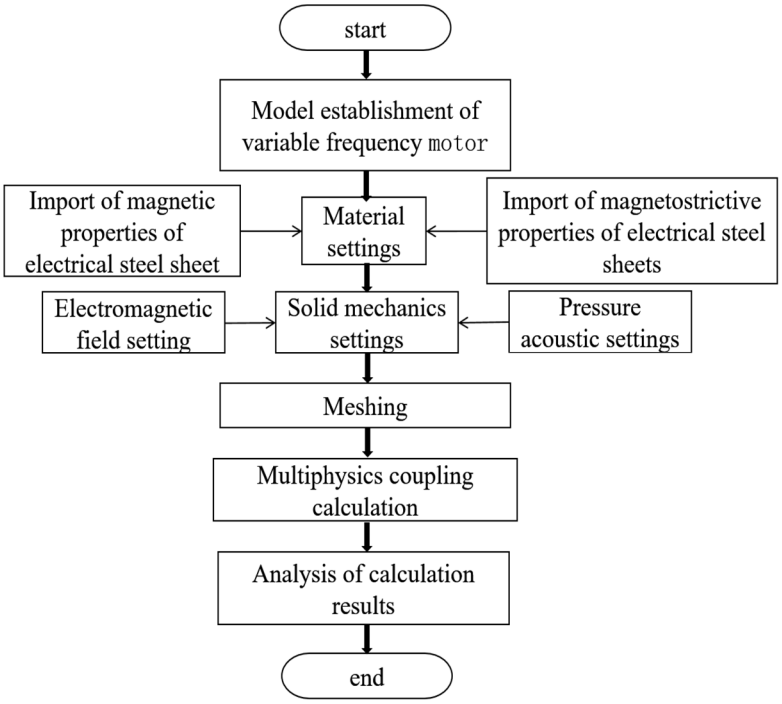


Figure 12. Finite element analysis flowchart.

4.1. Analysis of Electromagnetic Characteristics of Variable-Frequency Motors under Different Temperature and Harmonic Conditions

According to the finite element analysis process shown in Figure 12, the electromagnetic characteristics of the variable-frequency motor at separate temperatures and harmonics were simulated and analyzed.

We set the fundamental frequency of the induction motor at 50 Hz, 100 Hz, the third harmonic 150 Hz, and the fifth harmonic 250 Hz. The finite element analysis of the induction motor's electromagnetic force and noise during operation was carried out.

Figure 13 shows the magnetic induction intensity distribution of the variable-frequency motor at different temperatures. Figure 14 shows the distribution of the magnetic induction intensity of the down-conversion motor with diverse harmonics.

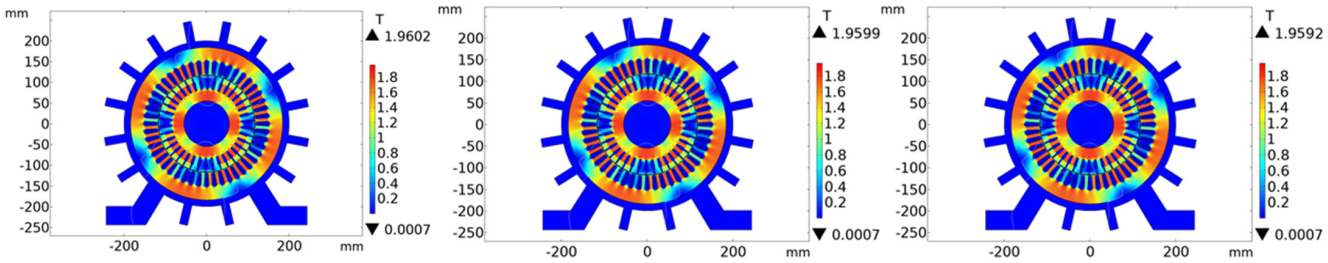


Figure 13. Magnetic field distribution of motor at diverse temperatures: (**a**) magnetic field distribution at 20 °C; (**b**) magnetic field distribution at 80 °C; (**c**) magnetic field distribution at 120 °C.

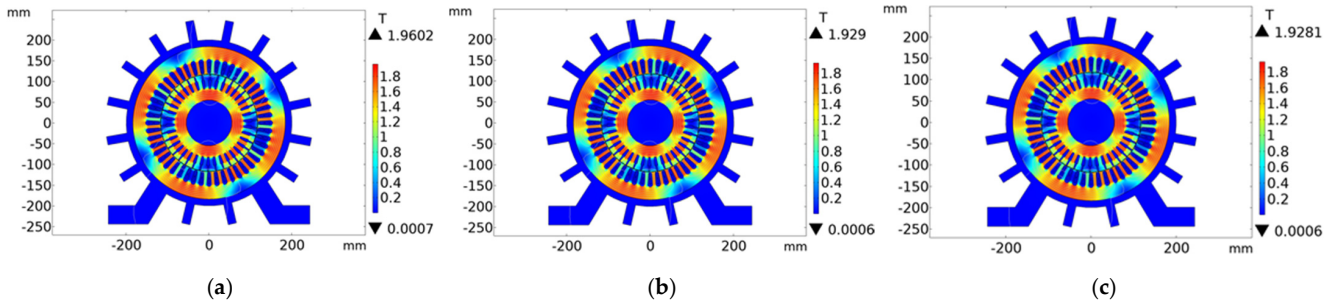


Figure 14. Magnetic field distribution of motor at diverse frequencies: (**a**) magnetic field distribution at 50 Hz; (**b**) magnetic field distribution at 150 Hz; (**c**) magnetic field distribution at 250 Hz.

As shown in Figure 13, as the test temperature of silicon steel sheets proliferates, the internal magnetic induction intensity of the motor decreases to a certain extent. However, in the process of motor design and performance research, it is generally the case that the magnetic induction intensity data are acquired at room temperature. Therefore, the influence of the silicon steel sheet test temperature on the performance of the motor should be considered when analyzing and designing the motor.

As shown in Figure 14, as the test frequency of the silicon steel sheets increases, the internal magnetic induction intensity of the motor decreases, which will lead to a change in motor loss, temperature, and other parameters, especially a change in motor performance under a variable-frequency power supply.

4.2. Analysis of Vibration Characteristics of Variable-Frequency Motor Considering Magnetostriction Effect

To investigate the influence of silicon steel sheet magnetostriction on the vibration of the variable-frequency motor, based on the COMSOL finite element analysis software, we proposed a finite element analysis model of motor vibration considering the magnetostriction of the silicon steel sheet. Figure 15 shows the vibration calculation process of the

1140 V/75 kW variable-frequency motor. As shown in Figure 16, the vibration deformation of the variable-frequency motor without considering the effect of magnetostriction was investigated, and Figure 17 presents the vibration deformation of the variable-frequency motor considering the effect of magnetostriction.

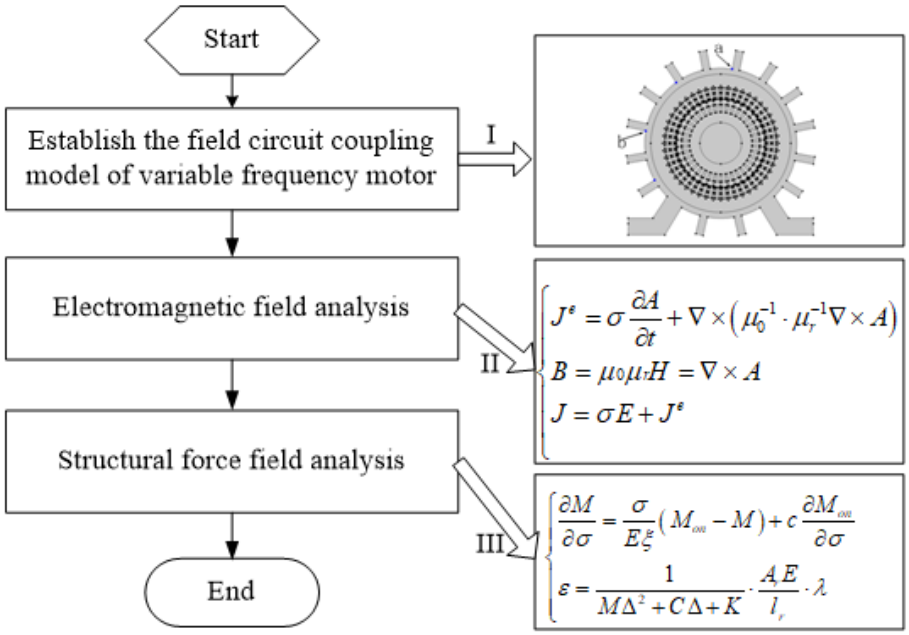


Figure 15. Calculation process of the motor.

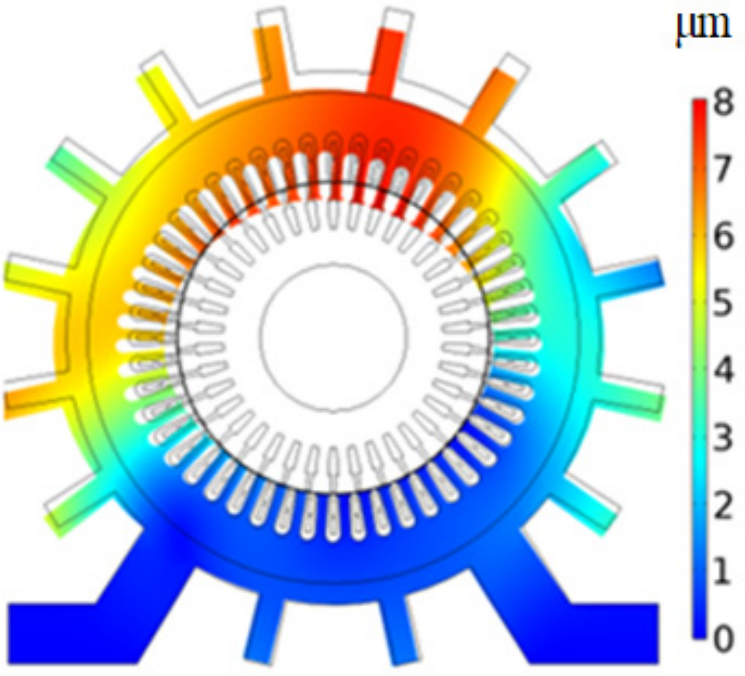


Figure 16. Vibration distortion of a motor not considering magnetostriction.

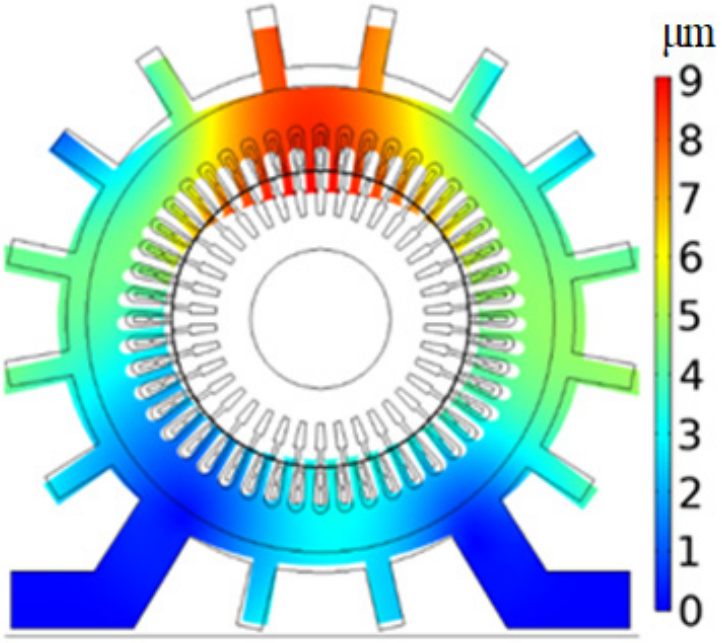


Figure 17. Vibration distortion of a motor considering magnetostriction.

In Figure 15, μ_0 is the vacuum permeability, μ_r is the relative permeability, A is the vector magnetic potential, J is the current density, E is the electric field strength, and "$\times$" represents the curl calculation symbol.

M is the mass matrix, C is the damping matrix, K is the stiffness matrix, ξ is the damping ratio, Δ is the partial derivative of displacement to time, λ is the deformation variable, σ is the stress, ε is the strain, I_r is the energy functional, and "$\cdot$" represents the divergence calculation symbol.

As shown in Figure 17, the vibration displacement of the induction motor is asymmetric under the bottom constraint and the maximum displacement is 9 μm when considering the influence of magnetostriction.

The comparison of vibration displacement before and after considering the influence of magnetostriction is substantiated in Table 5.

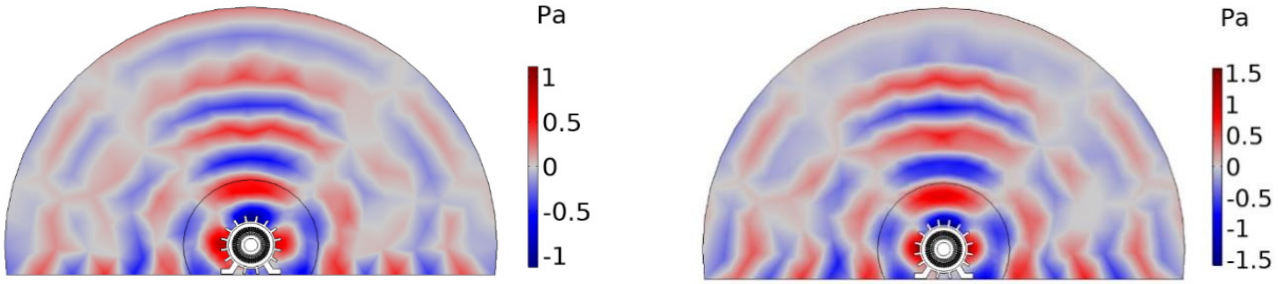
Table 5. Comparison of vibration displacement.

Project	Vibration Displacement/μm
Considering magnetostriction	8
Magnetostriction not considered	9

It can be obtained from Table 5 that the vibration displacement of the variable-frequency motor considering the influence of magnetostriction is larger than that without considering the influence of magnetostriction.

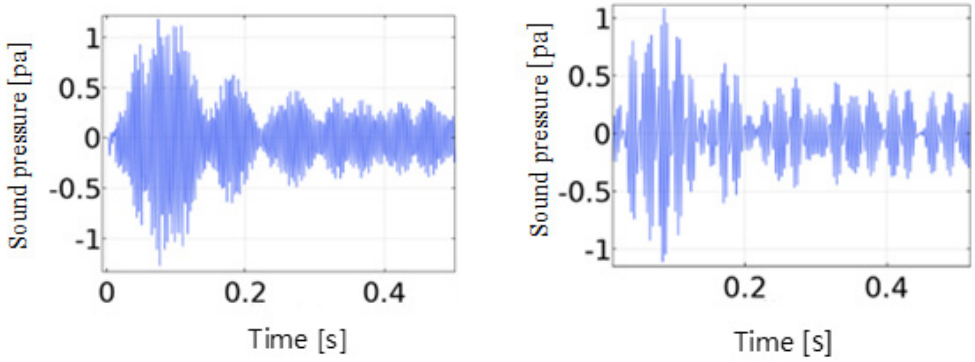
This is mainly due to the alternating magnetic field. The vibration of the iron core is mainly caused by the magnetostrictive effect of the ferromagnetic material, i.e., the size of the silicon steel sheet increases along the direction of the magnetic field line, and the size of the silicon steel sheet decreases perpendicularly to the direction of the magnetic field line. Under the condition of frequency conversion, it complies with the ISO-1 standard.

After the coupling calculation, the sound field simulation results of the 1140 V/75 kW variable frequency motor were obtained, and the noise in the air area one meter away from the periphery of the motor was analyzed. Figures 18 and 19 shows the sound field distribution and sound pressure waveform before and after magnetostriction



(**a**) (**b**)

Figure 18. Sound field distribution before and after magnetostriction: (**a**) the sound field distribution when magnetostriction is not considered; (**b**) the sound field distribution when magnetostriction is considered.



(**a**) (**b**)

Figure 19. Sound pressure waveforms before and after magnetostriction: (**a**) before magnetostriction; (**b**) after magnetostriction.

Through the analysis of the results ofFigures 18 and 19, it can be seen that the sound pressure increases significantly after adding the influencing factors of the magnetostriction effect. The specific data comparison is substantiated in Table 6.

Table 6. Comparison of acoustic data before and after magnetostriction.

	Magnetostriction Not Considered	**Considering Magnetostriction**
Sound pressure level/Pa	0.306	0.35
Noise/dB	83.6	84.8

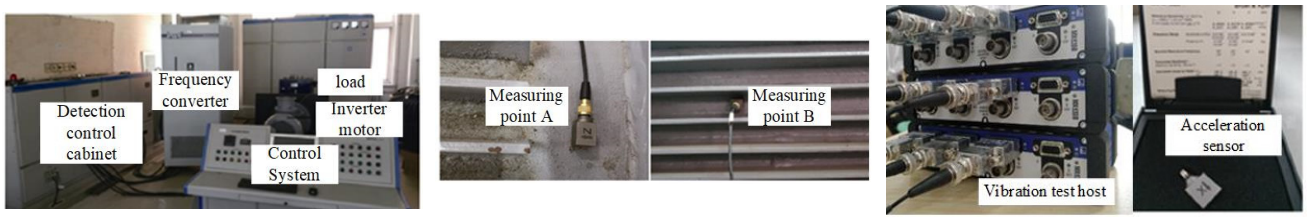
5. Experiment on the Vibration Characteristics of Variable-Frequency Motor

With the aim of verifying the correctness of the scheme proposed in this paper, an experimental investigation was carried out on the vibration of the 1140 V/75 kW variable-frequency motor. Figure 16 shows the variable-frequency motor experimental system.

During the experiment, the induction motor had a rated voltage of 1140 V, a rated current of 54 A, a rated speed of 1478 rpm, and a rated frequency of 50 Hz. We measured the vibration of the motor at 5 Hz, 25 Hz, and 50 Hz. Each measuring point was measured 5 times, one maximum value was removed, one minimum value was removed, and the error of the other three values was controlled within 5% as the actual measurement result.

As shown in Figure 20a, the test platform mainly included variable-frequency motors, loads, detect and control systems, frequency converters, etc. Figure 20b shows the vibration test points of the variable-frequency motor. Point A is at the end from the motor shaft side, and point B is concentrated in the middle of the motor. Figure 20c shows the vibration

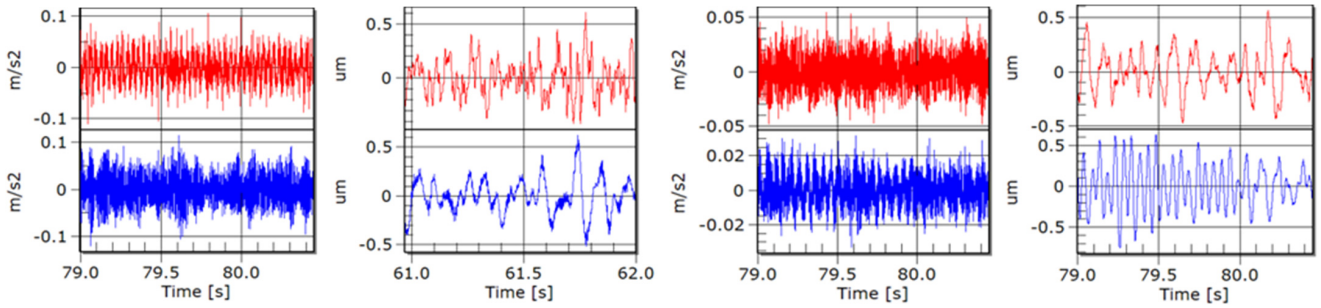
test instrument of the variable-frequency motor. The host used HBM's MX410 B, and the vibration acceleration sensor used BK's 4525-B.



(**a**) (**b**) (**c**)

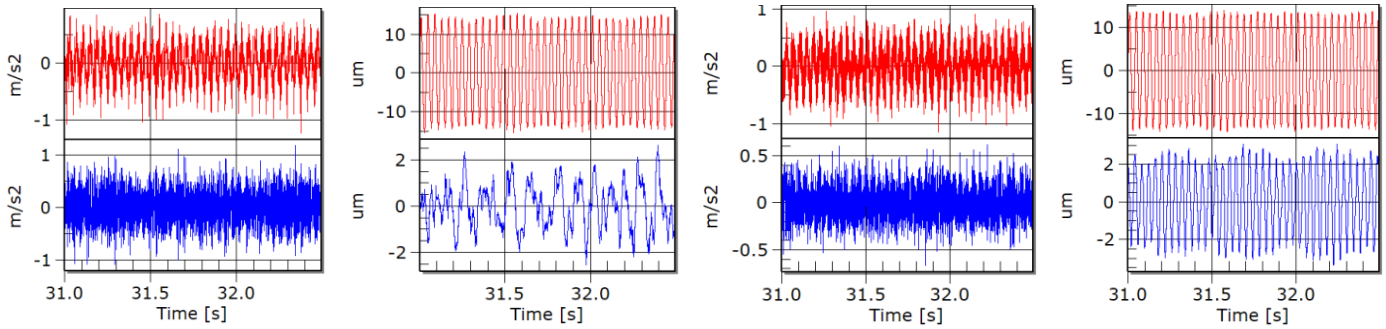
Figure 20. Experimental system of variable-frequency motor: (**a**) testing platform; (**b**) measuring point position; (**c**) test instrument.

Figures 21–23 show the vibration acceleration and displacement curves of point A and point B of the variable-frequency motor at 5 Hz, 25 Hz, and 50 Hz.



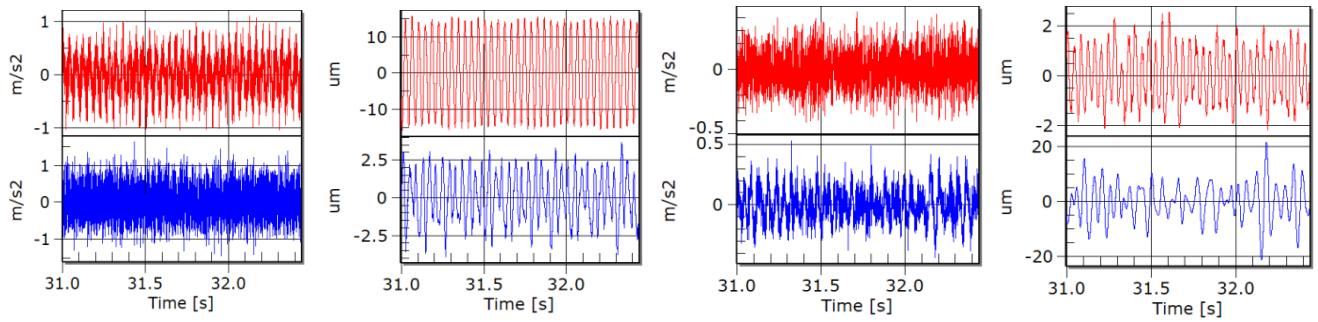
(**a**) (**b**) (**c**) (**d**)

Figure 21. Acceleration and displacement curve of point A and B in X/Y direction at 5 Hz: (**a**) acceleration curve of point A; (**b**) displacement curve of point A; (**c**) acceleration curve of point B; (**d**) displacement curve of point B.



(**a**) (**b**) (**c**) (**d**)

Figure 22. Vibration acceleration and displacement curves of points A and B at 25 Hz: (**a**) acceleration curve of point A; (**b**) displacement curve of point A; (**c**) acceleration curve of point B; (**d**) displacement curve of point B.



(**a**) (**b**) (**c**) (**d**)

Figure 23. Vibration acceleration and displacement curves of points A and B at 50 Hz: (**a**) acceleration curve of point A; (**b**) displacement curve of point A; (**c**) acceleration curve of point B; (**d**) displacement curve of point B.

As seen in Figures 21–23, the error between the measured vibration displacement data of the variable-frequency motor and the vibration displacement curve was obtained by the curve error of an order of magnitude, consistent trend, and qualitative analysis of the vibration trend of variable-frequency motors. There are two reasons for the error: (1) in the simulation process, the variable frequency motor is an ideal model; however, in the experiment, the variable-frequency motor was constrained by the bottom and was connected with the accompanying motor through a flexible coupling, which increased the error; (2) the measuring instrument experienced measurement error.

6. Conclusions

We studied the electromagnetic characteristics and vibration characteristics of the 1140 V/75 kW variable-frequency motor and drew the following conclusions:

(1) From the point of view of motor materials, the electromagnetic properties and magnetostrictive properties of the silicon steel sheet were measured and analyzed. We observed from the results that, with the increase in temperature and harmonics, the working performance of the DW315-50 silicon steel sheet becomes worse. With the increase in the measured induction strength of the silicon steel sheet, the single-value magnetostriction of the DW315-50 silicon steel sheet gradually increases and tends towards saturation, and its maximum magnetostriction is 4000 nm/m.

(2) The vibration of the 1140 V/75 kW variable-frequency motor was programmed and calculated using the traditional analytical method. The force wave order of the ratio of stator 48 slots and rotor 38 slots was analyzed. After analytical calculation, the air gap magnetic induction intensity of the 1140 V/75 kW variable-frequency motor was 1.1 T, and the maximum vibration displacement of the motor stator was 10 μm.

(3) The simulation modeling of the 1140 V/75 kW variable-frequency motor was completed, and, based on COMSOL finite element simulation software, the coupling analysis of the electromagnetic field, mechanical field, and sound field was completed, and the influence of magnetostriction on vibration was considered. Through simulation calculation, the vibration displacement was found to be 18 μm and the sound pressure was 0.35 Pa.

(4) An experimental platform was built for the vibration test of the 1140 V/75 kW variable-frequency motor, and its vibration acceleration and vibration displacement were collected and analyzed. The maximum vibration displacement was 20 μm, which verified the scheme proposed in this paper.

It is of great significance to investigate the magnetic properties of the stator core materials of variable-frequency motors resulting in various temperatures and harmonics. When calculating the vibration and noise of variable-frequency motors, considering the influence of the magnetostrictive effect will make the results more accurate and play a guiding role in optimizing motor design.

Author Contributions: Writing—original draft, Z.S.; Writing—review & editing, L.L., J.L., Z.L., H.L. and H.B. All authors have read and agreed to the published version of the manuscript.

Funding: This research received no external funding.

Institutional Review Board Statement: Not applicable.

Informed Consent Statement: Written informed consent has been obtained from the patient(s) to publish this paper.

Conflicts of Interest: The authors declare no conflict of interest.

References

1. Bai, B.D.; Chen, D.Z.; Wang, X.B. IGBT loss calculation and cooling device design of inverters. *J. Electr. Technol.* **2013**, *28*, 97–106.
2. Mohammed, O.A.; Calvert, T.E.; Mcconnell, R. Coupled magnetoelastic finite element formulation including anisotropic reluctivity tensor and magnetostriction effects for machinery applications. *IEEE Trans. Magn.* **2001**, *37*, 3388–3392. [CrossRef]
3. Fan, W.; Yang, Y.; Su, X. Dynamic Modeling and Vibration Characteristics Analysis of Transmission Process for Dual-Motor Coupling Drive System. *Symmetry* **2020**, *12*, 1171. [CrossRef]
4. Maraaba, L.S.; Twaha, S.; Memon, A.; Al-Hamouz, Z. Recognition of Stator Winding Inter-Turn Fault in Interior-Mount LSPMSM Using Acoustic Signals. *Symmetry* **2020**, *12*, 1370. [CrossRef]
5. Chang, Y.H.; Hsu, C.H.; Chu, H.L.; Tseng, C.P. Magnetomechanical vibrations of three-phase three-leg transformer with different amorphous-cored structures. *IEEE Trans. Magn.* **2011**, *47*, 2780–2783. [CrossRef]
6. Mohammed, O.A.; Abed, N.Y.; Liu, S.; Ganu, S. Acoustic noise signal generation due to magnetostrictive effects in electrical equipment. In Proceedings of the Twenty-Second National Radio Science Conference, 2005, NRSC 2005, Cairo, Egypt, 15–17 March 2005; Volume 1, pp. 45–52.
7. Delaere, K.; Heylen, W.; Belmans, R.; Hameyer, K. Comparison of induction machine stator vibration spectra induced by reluctance forces and magnetostriction. *IEEE Trans. Magn.* **2002**, *38*, 969–972. [CrossRef]
8. Islam, M.; Islam, R.; Sebastian, T. Noise and vibration characteristics of permanent-magnet synchronous motors using electromagnetic and structural analyses. *IEEE Trans. Ind. Appl.* **2014**, *50*, 3214–3222. [CrossRef]
9. Fodorean, D.; Husar, C.; Irimia, C. Noise and vibration behavior evaluation of dc motor and pmsm in electric traction application. In Proceedings of the 2016 International Symposium on Power Electronics, Electrical Drives, Automation and Motion (SPEEDAM), Capri, Italy, 22–24 June 2016; pp. 1184–1189.
10. Gao, L.; Zheng, H.; Zeng, L.; Pei, R. Evaluation method of noise and vibration used in permanent magnet synchronous motor in electric vehicle. In Proceedings of the 2019 IEEE Transportation Electrification Conference and Expo (ITEC), Detroit, MI, USA, 19–21 June 2019; pp. 1–4.
11. Zhang, W.; Xu, Y.; Huang, Y.; Zou, J. Reduction of high-frequency vibration noise for dual-branch three-phase permanent magnet synchronous motors. *Chin. J. Electr. Eng.* **2020**, *6*, 42–51. [CrossRef]
12. Deng, W.; Zuo, S. Axial Force and Vibroacoustic Analysis of External-Rotor Axial-Flux Motors. *IEEE Trans. Ind. Electron.* **2018**, *65*, 2018–2030. [CrossRef]
13. Han, Z.; Liu, J. Comparative Analysis of Vibration and Noise in IPMSM Considering the Effect of MTPA Control Algorithms for Electric Vehicles. *IEEE Trans. Power Electron.* **2021**, *36*, 6850–6862. [CrossRef]
14. Li, D.; Zhang, Y.; Li, M.; Zhang, D.; Koh, C.S. Study on the Vibration and Noise of PMSM By Considering the Vector Magnetostrictive Property in a Non-Oriented Silicon Steel Sheet. In Proceedings of the 2020 23rd International Conference on Electrical Machines and Systems (ICEMS), Hamamatsu, Japan, 24–27 November 2020; pp. 1695–1698.
15. Cho, S.; Hwang, J.; Kim, C.-W. A Study on Vibration Characteristics of Brushless DC Motor by Electromagnetic-Structural Coupled Analysis Using Entire Finite Element Model. *IEEE Trans. Energy Convers.* **2018**, *33*, 1712–1718. [CrossRef]
16. Bo, Y.; Li, S.; Hu, G. Research on electromagnetic force wave analysis and vibration characteristics of permanent magnet synchronous motor based on finite element simulation. In Proceedings of the 2020 IEEE 3rd International Conference of Safe Production and Informatization (IICSPI), Chongqing, China, 28–30 November 2020; pp. 192–196.